Extreme Mechanics Letters 68 (2024) 102140

Contents lists available at ScienceDirect

Extreme Mechanics Letters

journal homepage: www.elsevier.com/locate/eml

Progressive adhesion mechanics of elastomeric shells against a rigid substrate: From thin to thick

Chenxu Zhao [a], Kai-tak Wan [b,*], Wanliang Shan [a,*]

[a] Mechanical Engineering, Syracuse University, NY, USA
[b] Mechanical & Industrial Engineering, Northeastern University, MA, USA

ARTICLE INFO

Keywords:
Shell
Adhesion
Pull-off
Elastomer
Large deformation

ABSTRACT

Hemispherical elastomeric shells with a range of thickness, h, press against a planar glass plate in the presence of interfacial adhesion. The applied load, P, is measured as a function of approach distance, δ, while the contact radius, a, is simultaneously monitored. Thick shells with thickness exceeding 3/10 of the hemispherical radius, R, behaves as the classical Hertz-JKR solid sphere, as manifested by the *pull-off* tensile force and contact radius. As the shell gets thinner, the detachment trajectory deviates and the pull-off force decreases. Very thin shells with h/R falling below 0.05, an uptick in adhesion is observed. Measurements are performed in shells fabricated in two common polymers. Experimental data are fairly consistent with computational results generated by finite element analysis.

1. Introduction

Adhesion is a ubiquitous phenomenon that is crucial in both engineering and natural systems. It finds applications in nano-/micro-electromechanical systems (N/MEMS) where it influences stiction [1,2], and dry-adhesion-based soft grippers where tunable adhesion is used to enable robotic manipulation [3–6]. A recent study shows that soft gripper design based on hollow pillar structures can significantly increase adhesion tunability that requires significantly lower activating pressure in operation [7]. Adhesion also plays crucial roles in biology, such as erythrophagocytosis, which involves the interaction between red blood cells and macrophages [8]. Another notable example is shell adherence that underlies cellular interactions, key to understanding of bacterial adhesion onto filters [9–12].

Intersurface forces in the context of solid-solid adhesion have been expounded by seminal theories by Johnson-Kendall-Roberts (JKR) [13], Derjaguin-Muller-Toporov [14], and Dugdale-Barenblatt-Maugis [15]. Membrane adhesion is also extensively investigated [16–19]. The JKR contact theory has been applied to slender shells under the assumption of minimal deformation using Reissner's shell theory [12,20]. Our recent work has explored the adherence of hyperplastic shells under large deformation using finite element modeling (FEM) based on Maugis' graphical method. While some studies have quantified the deformation of finite-thickness shells such as contact lenses [21], literature remains quite rare in adherence-detachment of shells. The present study focuses on hemispherical shells with thickness from very thin to very thick against a rigid planar substrate (Fig. 1). Critical tensile force (P^*) and contact radius (a^*) are measured under quasistatic conditions and slow loading rate and compared to the JKR solid sphere limit. Data are analyzed based on FEM [22]. We will highlight the difference of a shell compared to a solid sphere and pillars with flat contact surfaces and discuss the implications in design of shell-shaped soft grippers.

2. Materials and methods

2.1. Materials and measurements

Two commercially available elastomer vinylpolysiloxane (VPS), namely, a relatively soft VPS-8 (Zhermack, Elite Double 8) and a relatively stiff VPS-32 (Zhermack, Elite Double 32) are used to prepare our sample shells, mainly because of their desirable mechanical properties and short curing time of approximately 15 minutes [23]. A mixing ratio of the reagents A:B = 1:1 is used. By compressing a solid hemisphere, the load-displacement relation is characterized and fitted by a neo-Hookean model assuming $E = 6\ C_1$. The Young's moduli of the as-fabricated samples are thus measured to be $E_{VPS-8} = 0.20 \pm 0.1$ MPa and $E_{VPS-32} = 0.87 \pm 0.1$ MPa. A piece of glass (United Scientific™ GLP2×2-S Glass Streak Plates) with dimensions of 2" × 2" × 1/4" serves as the substrate

* Corresponding authors.
E-mail addresses: ktwan@coe.neu.edu (K.-t. Wan), washan@syr.edu (W. Shan).

https://doi.org/10.1016/j.eml.2024.102140
Received 10 September 2023; Received in revised form 16 January 2024; Accepted 19 February 2024
Available online 21 February 2024

which is rigid upon adhesion and detachment of the soft shells. A high-resolution digital microscope (KH8700, Hirox) is used to examine the cross-section of the shells and to measure h and R. Fig. 1 shows the schematics of the detachment process. A hemispherical shell with an outer radius, $R = 10$ mm, and thickness, h, adheres to the substrate in the absence of external load. A thin shell has $(h/R) << 1$, whereas a solid hemisphere has $(h/R) = 1$. Normal tensile load, P, is then applied to shrink the contact area and ultimately detach the shell from the substrate. Experiments are conducted for shells with a range of h.

Shells are fabricated using two different methods. Shells with $h >$ 1 mm are made by casting the raw materials in a 3-D printed VeroWhite mold (Objet24, Stratasys Inc.). The mold comprises complementary concave-convex parts with a uniform gap of h. The elastomer reagent is poured to fill the gap between the concentric surfaces and cured to form the sample shell as shown in Fig. 2a. It is quite challenging to make very thin shells with $h < 1$ mm using the same method because of the inevitable imperfections and grain size in the 3D-printed mold. An alternative method single-mold direct coating is adopted [24]. The chemical reagent is poured onto the concave surface of a 3D-printed VeroWhite mold. The liquid film drains and thins out due to gravity. Curing takes place on the curved surface for more than 15 min. Despite the crude methods, sample shells exhibit remarkable uniform thickness with a variance less than 6.6% along the meridional direction from the pole to the rim. Further adjustment of the shell thickness can be achieved by varying the rheological properties of the reagent such as partially curing prior to casting. Thicker shells can be made by multiple coating and curing using the same mold.

Intrinsic imperfection and surface roughness of the 3D printed molds are unavoidable due to the limited resolution of the 3D printer. To ensure consistency in measurement, an additional 100 – 200 μm thick coating is applied after the shells are released from the molds. Surface tension of the liquid and gravity thus leave a smooth surface. Measurements show that with the additional coating layer thickens the shell of diameter $R = 10$ mm by 100–200 μm to within 1–2% among the samples. This level of consistency in shell thickness ensures reliability and repeatability and minimizes variations due to shell imperfection.

Fig. 2b shows the experimental setup. A shell is affixed onto a custom 3D-printed holder, which is attached to a 5 N load cell via a pneumatic gripper integrated into a universal testing machine, Instron 5969. The shell is then compressed against a glass plate firmly clamped in a 3D-printed frame. Upon compression, the applied load, P, is continuously monitored as a function of the approach distance, δ, and time, t. An LED light source is used to illuminate the contact interface to enhance image quality. A digital microscope, Celestron-5MP, positioned below the glass plate captures the in-situ images of the contact circle. Recorded videos are analyzed using the image processing software ImageJ.

The shell is initially brought into adhesive contact with the substrate by applying a compression at a loading rate of 1 mm/min until a preset distance is reached. To bring the shell sample and the glass substrate into contact without damaging the load cell by the preload, the preset distance is chosen to be $\delta = 1$ mm for VPS-8 shells and, $\delta = 0.5$ mm for VPS-32 shells. The adherends are maintained at the designated δ for 30 seconds to ensure intimate contact over the entire contact interface. As compression proceeds, the contact area expands and the contact radius, a, increases. The shell is then retracted from the substrate at an unloading rate of 0.2 mm/min as P diminishes and turns tensile. Once a critical threshold is reached at P^*, pull-off occurs and the shell spontaneously detaches from the substrate and a reduces to zero. The surface energy to separate a unit area of the shell-substrate interface is denoted by γ, which can be measured using a solid VPS hemisphere against the same glass substrate. Adhesion measurements are also performed for loading speed of 0.10, 1.0, and 10 mm/min.

The classical JKR model requires pull-off to occur at $P^* = 3/2\ \pi\ R\ \gamma$. Once P^* is measured, γ can be found accordingly. Based on three tests on six samples for each VPS sample, measurements yield $\gamma_{VPS\text{-}8} = 106 \pm 6$ mJ/m^2 and $\gamma_{VPS\text{-}32} = 125 \pm 10$ mJ/m^2.

2.2. Computational model

Two different theoretical models are readily available to interpret the experimental results [12,22]. The first is based on the Maugis' graphical method and FEM [22]. The total energy of the system, U_T, is the sum of the elastic energy stored in the shell, $U_E = \int P\, d\delta$, the potential energy due to the external load, $U_P = -P\ \delta$, and the surface energy, $U_S = \gamma\ \pi\ a^2$. The commercial software ABAQUS, with the CAX4RH element, generates the relation $P(\delta)$ for a range of fixed a, and thus yields U_T. Thermodynamic equilibrium is attained by putting $dU_T / da = 0$ and stable equilibrium requires $d^2U_T / da^2 > 0$. Detailed information is provided in Supplementary Information (Figure S3). Large deformation of VPS is here taken to be an incompressible neo-Hookean solid with the strain energy density function given by

$$W = C_1\left(\lambda_1^2 + \lambda_2^2 + \lambda_3^2 - 3\right) \tag{1}$$

where $C_1 = 0.033$ MPa for VPS-8 and $C_1 = 0.145$ MPa for VPS-32. Computation shows radial bulging slightly below the shell rim which is anchored to the sample holder.

The second model is based on an elastic spherical shell being com-

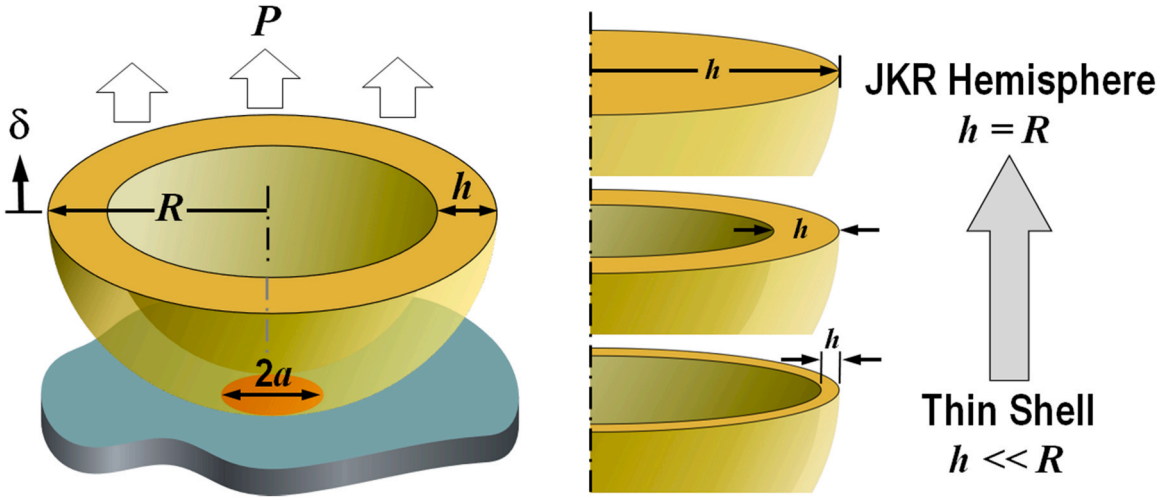

Fig. 1. Schematics of a hemispherical shell with thickness h and radius R adhered to a rigid plate creating a contact circle with radius a in the presence of external load P and adhesion. As the h approaches R, the shell behavior tends to the JKR limit.

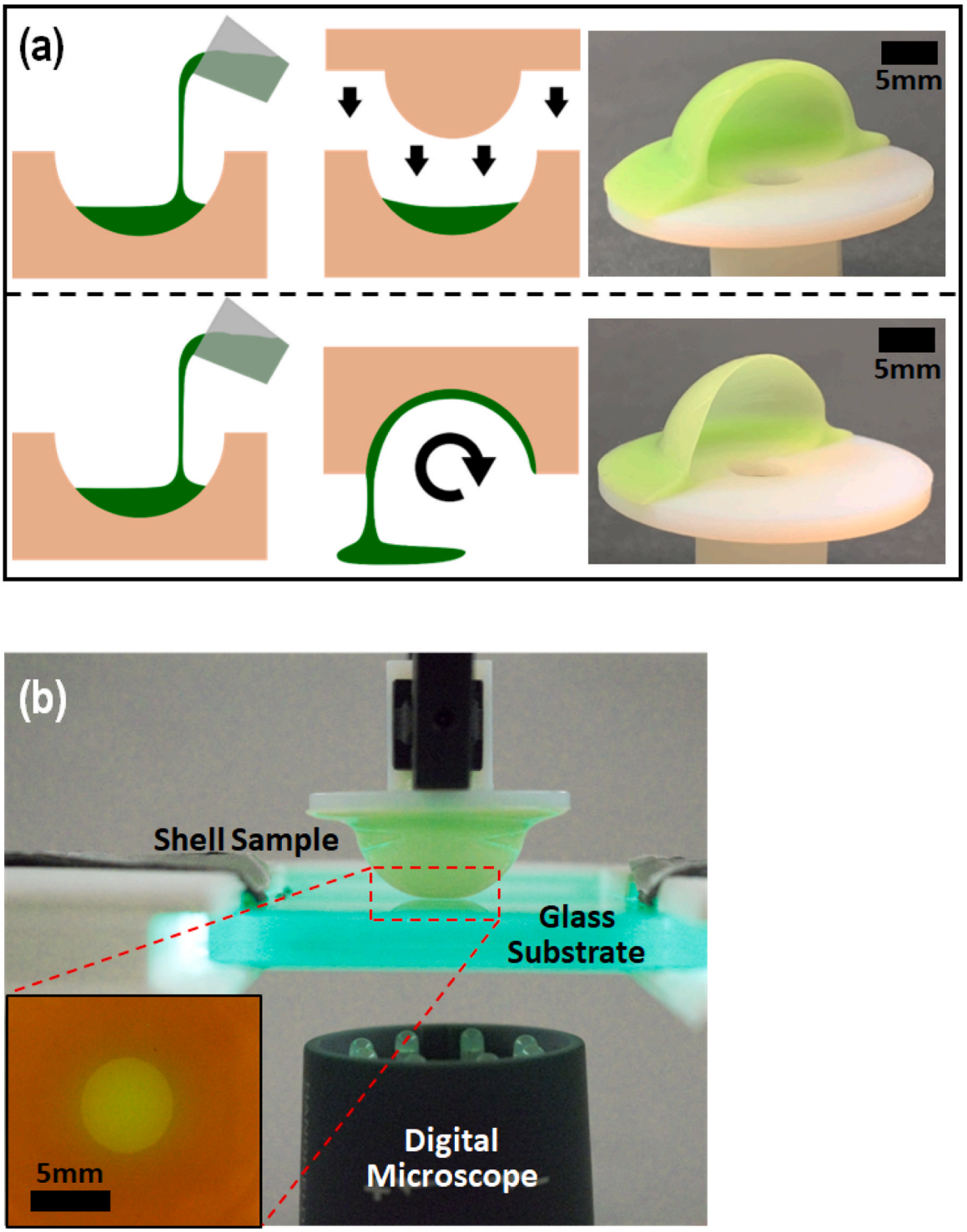

Fig. 2. (a) Schematic of the two fabrication methods and photographs of VPS-32 shell samples with different thicknesses. (b) Experimental setup for adhesion measurement.

pressed by two parallel plates in the literature [12]. Upon compression, symmetry requires bulging at the equator rather than below the equatorial rim as in the present work. Theoretical predictions from the two model are expected to be close, though they cannot be compared directly. It is nonetheless interesting to make a comparison. A finite difference method is employed to obtain the deformed shell profile and contact mechanics. Large deformation of mixed plate bending and membrane stretching is considered but not shearing. The shell material is assumed to be linear elastic. Following an energy balance based on the JKR model, the pull-off force of a thin shell is estimated to be:

$$P^* = \eta\left(\frac{\gamma^4 R^4(1-\nu^2)}{Eh^2}\right)^{1/3} \tag{2}$$

with E the elastic modulus and ν the Poisson's ratio of the shell material, and $\eta = 13.2 \pm 0.6$. A thinner shell with small h is expected to lead to a large P^*.

3. Results and discussion

The mechanical response of shell detachment, $P(\delta,a)$ and the pull-off parameters are measured as functions of shell thickness and material properties. Dynamic behavior in shells with a range of shell thickness is also investigated.

3.1. Detachment trajectory

Fig. 3a compares measurement with numerical results of $a(P)$ for a VPS-32 solid hemisphere upon unloading and ultimate detachment from the substrate. At $P = 0$, a contact circle with a finite radius a_0 (> 0) is measured. As the external load turns tensile to reach the critical threshold, P^*, the approach distance increases to δ^* and the contact circle shrinks to a^* (> 0). An incremental increase in P now triggers *pull-off* under fixed-load and the contact spontaneously shrinks to null. In the present work, experiments are performed under fixed-grips such that δ, rather than P, is controlled. Shrinkage of contact circle proceeds as in fixed-load along $P(\delta)$ in a quasistatic manner. However, pull-off does not occur at (P^*, δ^*, a^*) but delay till $\delta^\dagger$ ($> \delta^*$) with the corresponding $P^\dagger$ ($< P^*$) and $a^\dagger$ ($< a^*$). As shown in Fig. 3a, P reaches a maximum at $P^*(\delta^*)$ but begins to decrease as unloading continues till $P^\dagger(\delta^\dagger)$. In the JKR model and FEM simulations, the experimentally measured bulk material elastic modulus of VPS-32 ($E = 0.87$ MPa) leads to an overestimation of

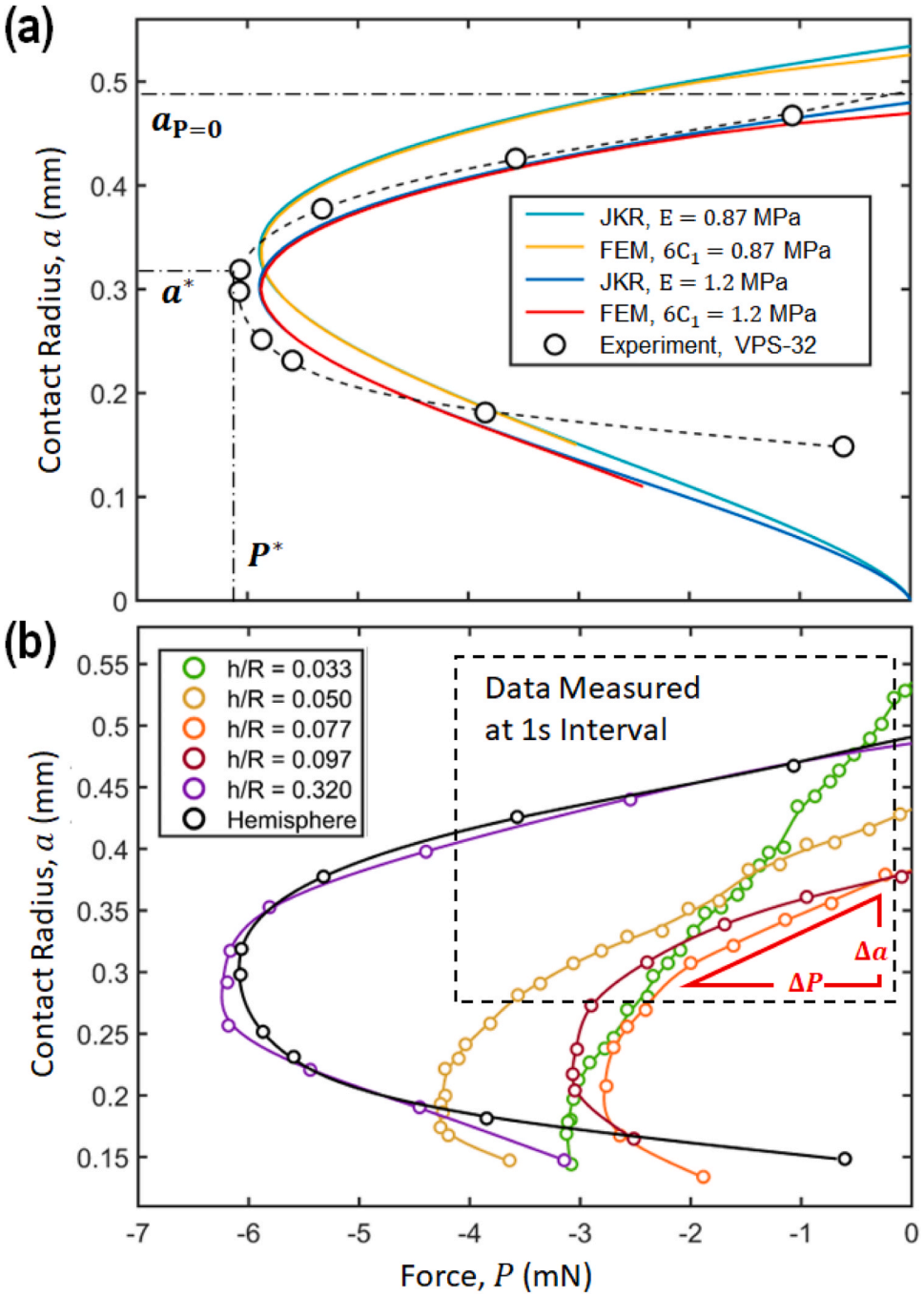

Fig. 3. Adhesion of VPS-32 shells at a constant retraction speed of 0.2 mm/min. (a) Solid hemisphere adhesion: contact radius a as a function of external tension P. Fixed-load pull-off force P^* and radius a^*, and radius a_0 at zero load are shown. (b) Adhesion-detachment of hemispherical shells, $a(P)$, for a range of shell thicknesses and h/R.

the contact radius a. This overestimation is attributed to the realignment of polymer chains during the surface coating process [25], which results in a hardened surface (Figure S1). In this study surface coating is utilized to achieve a consistently smooth surface as described in Section 2.1. It is expected that this surface coating can mitigate the effects of mold roughness and ensuring consistent surface energy across samples of the same material. However, this surface coating process introduces uncertainties in the elastic modulus near the shell surface. In our FEM simulations, we opted for simplicity by assuming a uniformly distributed elastic modulus across the thickness direction and continued to use the bulk material modulus in our analysis. As shown in Fig. 3a, using the bulk material modulus ($E = 0.87$ MPa), rather than assuming a larger modulus ($E = 1.2$ MPa) to compensate for surface hardening, leads to an overestimated contact radius in a solid sphere. Fig. 3b shows $a(P)$ for

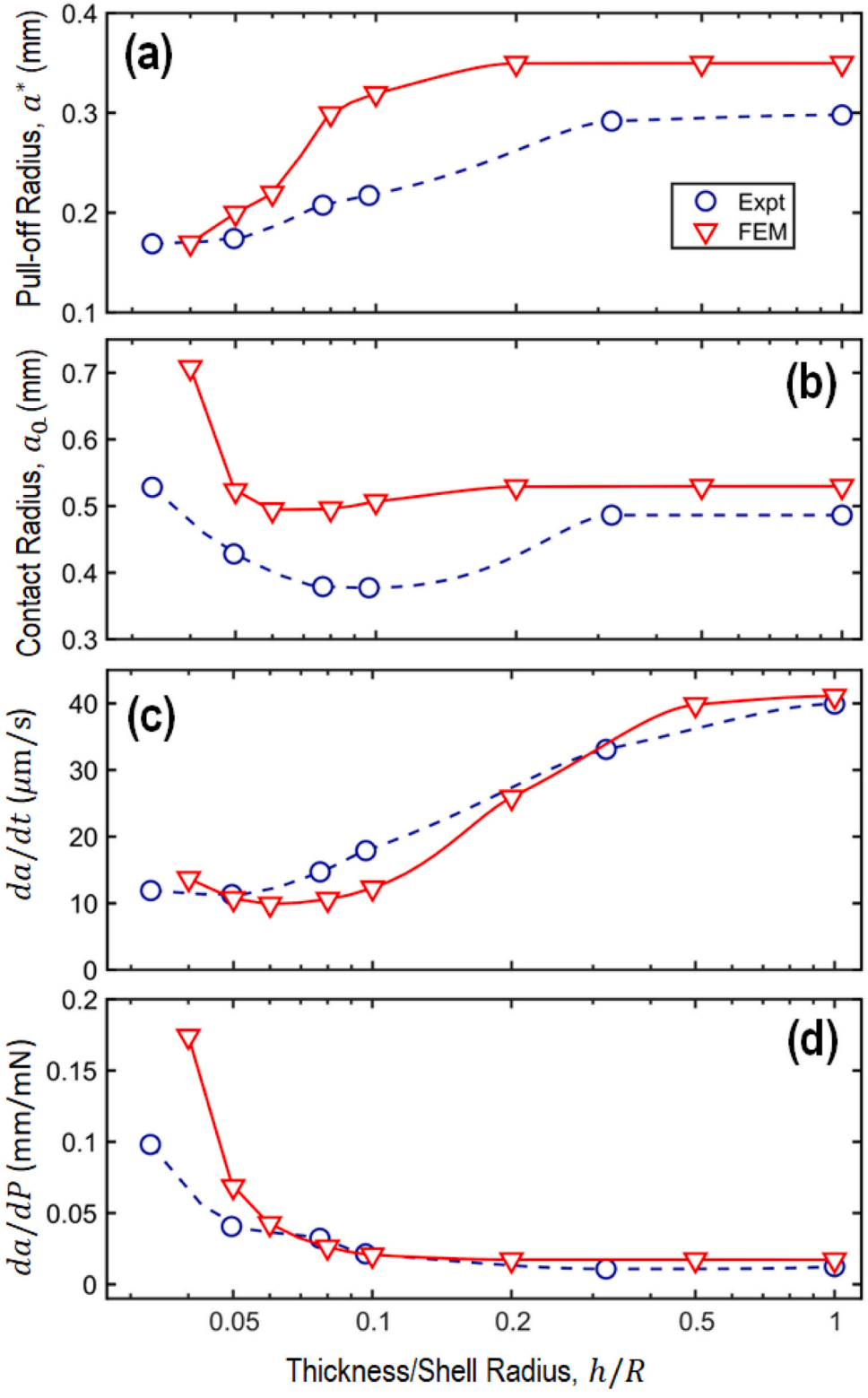

Fig. 4. VPS-32 shells at a constant retraction speed of 0.2 mm/min showing a^*, a_0, da/dP, and da/dt as functions of shell thickness. Data are extraction from Fig. 3b.

VPS-32 shells with a range of thickness. The general trends such as shrinking contact circle as tensile load increases, triggering fixed-load pull-off at critical maximum load, and fixed-grips pull-off at the maximum approach distance, as quite similar to the JKR solid. In fact, behavior of a thick shell with $(h/R) = 0.32$ almost replicates a JKR hemisphere. As the shell gets thinner, the detachment trajectory deviates further from the JKR limit. Critical points such as a^* and a_0 are extracted from the measurement and plotted in Fig. 4(a-b). A thinner shell gives rise to a monotonically decreasing $a^*(h)$ from the JKR limit with the transition at $(h/R) \approx 0.20$. On the other hand, $a_0(h)$ decreases initially, but drastically increases as thickness falls below $(h/R) \approx 0.06$. These trends are qualitatively consistent with FEM. Figure S2 illustrates that in a thin shell scenario, an increase in modulus results in a larger a_0, while a^* remains roughly constant. Furthermore, based on the findings

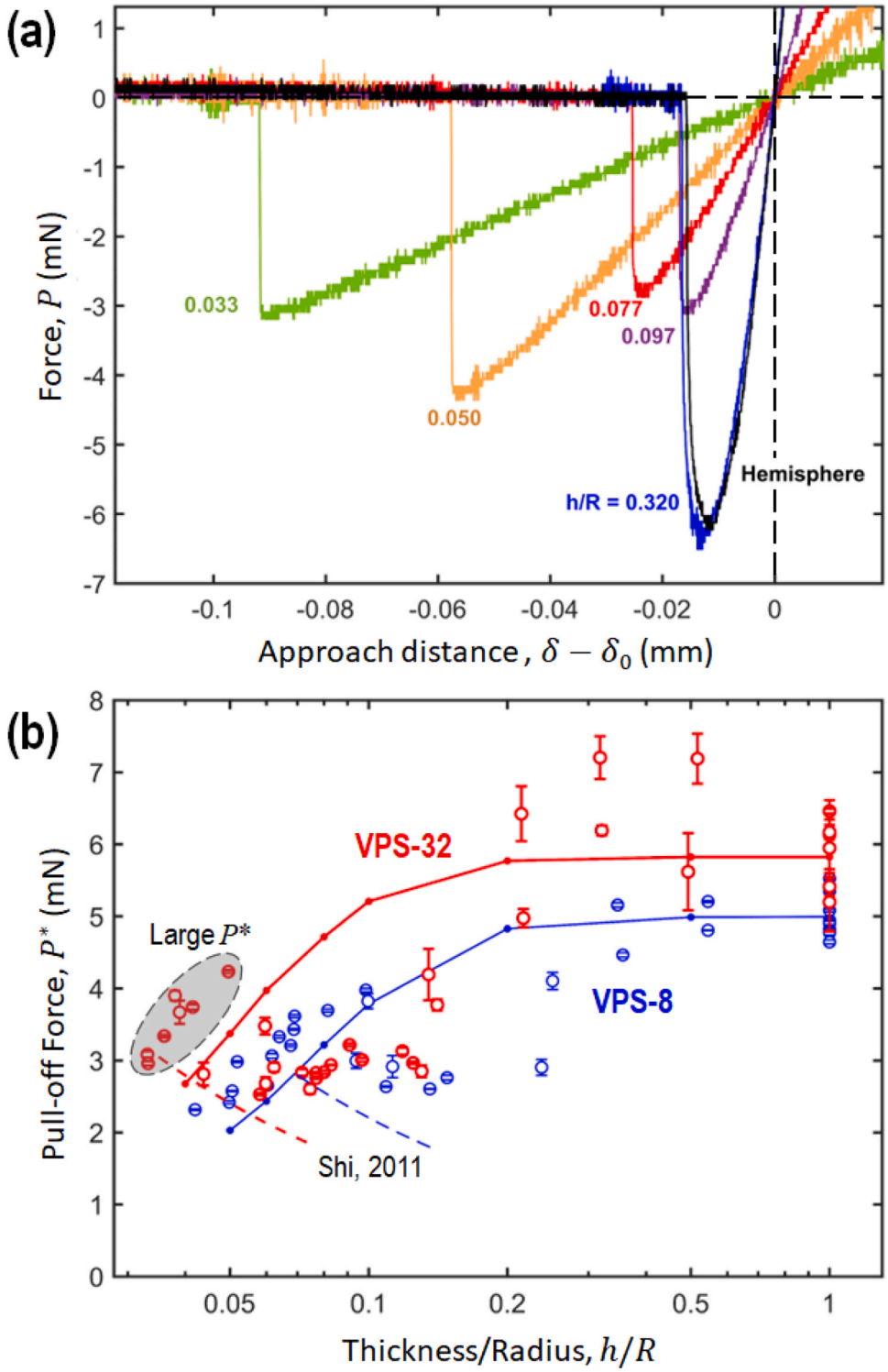

Fig. 5. (a) External tension as a function relative displacement ($\delta - \delta_0$) during unloading for a range of shell thickness, with δ_0 the approach distance at $P = 0$. (b) Pull-off force as a function of shell thickness: measurements are shown as symbols, FEM results as solid curves, and theoretical prediction as dashed curves. Shaded region indicates a sudden augmentation in P^*. The maximum pre-load displacement for VPS-32 and VPS-8 are 0.5 mm and 1 mm correspondingly.

presented in Fig. 3a and Figure S2, the deviations observed in Fig. 4(a-b) can be attributed to the surface hardening of the shell samples. It is remarkable that the large a_0 for shell with $h/R = 0.033$ signifies a slow increase in contact as the compliant thin shell conforms to the substrate geometry. The dashed box shown in Fig. 3b encircling data taken every second such that more data points indicate slower rate of contact radius shrinkage, da/dt, as shown in Fig. 4c. A solid sphere stores significantly more elastic energy upon deformation compared to a shell. An incremental increase in tensile load thus causes a large shrinkage in contact as expected. A shell is in general slower to respond to external load and stays longer in intimate contact with the substrate. Fig. 4d shows the corresponding mechanical response, da/dP, prior to fixed-load pull-off. In a thin shell, an incremental increase in tensile P leads to large contact shrinkage, since a large a_0 and small a^* yields a large $(a_0 - a^*)$. Conversely, a solid hemisphere leads to a small a_0 and large a^*, which yields a small $(a_0 - a^*)$.

Fig. 5a shows typical measurement of $P(\delta - \delta_0)$ with δ_0 the approach distance at zero external load, $P = 0$. Thin shells exercise large deformation and thus allow significantly large δ upon loading prior to pull-off. It is also noted that most set of data do not end at the maximum load P^* but δ continues to grow till the fixed-grips pull-off occurs. Fig. 5b shows the strong dependence of P^* upon h for the two elastomers. The stiffer VPS-32 shells require larger P^* to detach from substrate compared with the softer VPS-8. For thick shells with $(h/R) > 0.5$, P^*_{JKR} provides the upper bound as expected. As shells get thinner, P^* falls further below P^*_{JKR}, which qualitatively agrees with the JKR-based FEM results [22]. When a shell thins to $0.05 < (h/R) < 0.15$, the pull-off force falls in the range of $2.5 \leq P^* \leq 4.0$ (mN). As (h/R) falls below 0.05, P^* rises distinctly, especially in case of VPS-8, which is repeatable in multiple measurements, despite the difficulty to resolve the exact value of h when this occurs. Eq. (2) reflects the trend at least qualitatively as shown in Fig. 5b. FEM seems to be unable to capture this feature likely due to the following reasons. Only a single value of E or C_1 serves as input to FEM, which does not reflect the presence of a hardened surface coating. Since attraction is presence at the interface of this layer and the glass substrate, the stress field at the contact edge and the associated elastic energy stored in the multi-layered medium are not captured by FEM. Another limitation of FEM is the predicted bulging slightly below the equator that leads to an axisymmetric shear at the interface. The model leading to Eq. (2) also suffers from the same limitation. However, since the shell rim is free to bulge or expand radially, lateral shear at the contact is therefore minimized and pull-off occurs in opening mode I instead of mixed mode I & II [26]. In our experiment, external load applied at the rim is remote to the contact, and Eq. (2) seems to be a better representation of the loading configuration. Further investigation is necessary to verify the assumption.

3.2. Stress field

To better understand the transition from hemispherical solid to shell, normal stress at the crack tip for both $P = 0$ and $P = P^*$ is computed by FEM as shown in Fig. 6. In the presence of an ideal zero-range intersurface force, the opposite surfaces are pulled into an intimate contact resulting in a large tensile stress at the contact edge in reminiscent of the stress singularity in classical fracture mechanics. In case of a JKR solid ($h = R$), compression is always present within the central region of the contact circle as in classical Hertz contact theory. In the absence of external load, the central compression is balanced by the annular tension to reach mechanical equilibrium. Upon unloading, the compressed region reduces in both magnitude and volume but survives at pull-off. In case of a shell with intermediate thickness $(h/R) = 0.10$, the free inner shell surface gives rise to an image force of the contact stress, resulting in a reduced contact stress field in magnitude and volume. The phenomenon is more pronounced in very thin shell with $(h/R) = 0.04$. Upon contact with the substrate, the inverted dome is flattened to a plane and the geometrical deformation leads to compression with a minimum at the center. The apparent thin film now in contact with the substrate is under plane strain and the contact stress distributes uniformly and thinly over the now large contact circle at $P = 0$. In fact, mechanical stress is localized at the contact edge or crack tip where intersurface force acts. As unloading continues, the contact circle and the inner compression circle contract. At pull-off, compression virtually disappears within the entire contact circle leaving behind only tensile stress confined to a small annular at the contact edge. Equilibrium is established when the net intersurface force is balanced by the external P^*.

3.3. Influence of unloading speed

Viscoelasticity of the elastomers is linked to the adhesion-detachment responses in compliant robotic gripping systems [27,28] and is briefly investigated here. Dynamic measurements of P^* at small loading rates are performed. Fig. 7 shows the changing P^* as a function of the unloading speed $d\delta/dt$. As $d\delta/dt$ approaches zero, the measured P^* approaches the quasistatic limit. For practical purposes, $d\delta/dt =$

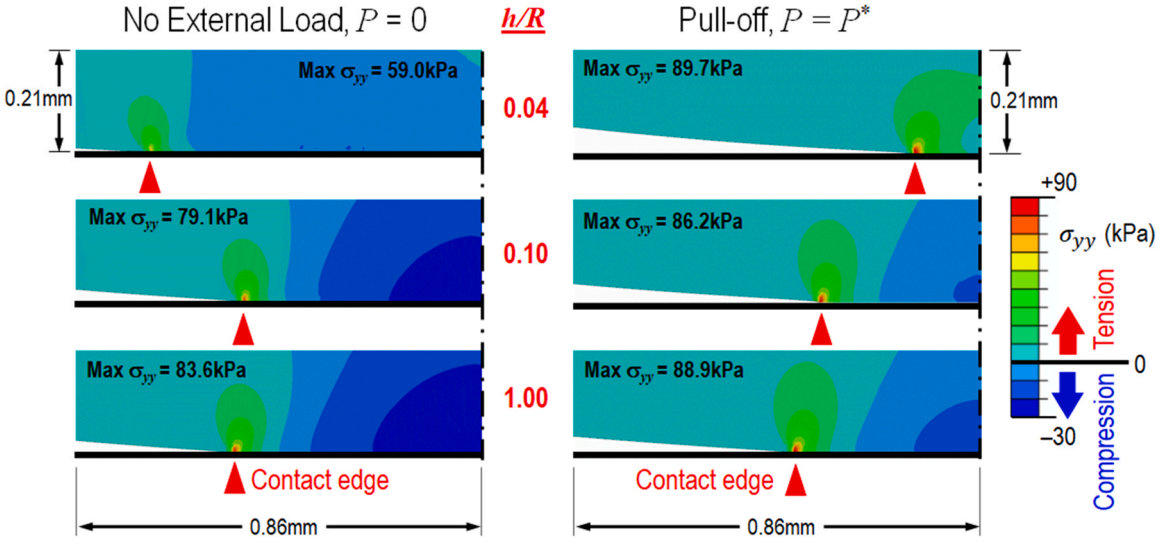

Fig. 6. Normal stress field from the contact center to the contact edge for shells with a range of thickness at zero external load and pull-off. Both compressive and tensile stresses in very thin shells are significantly smaller than that in a JKR solid hemisphere. In a thin shell, compressive stress is almost uniform within the contact at $P = 0$ but disappear at pull-off. Compression is always present in thick shell and JKR solid.

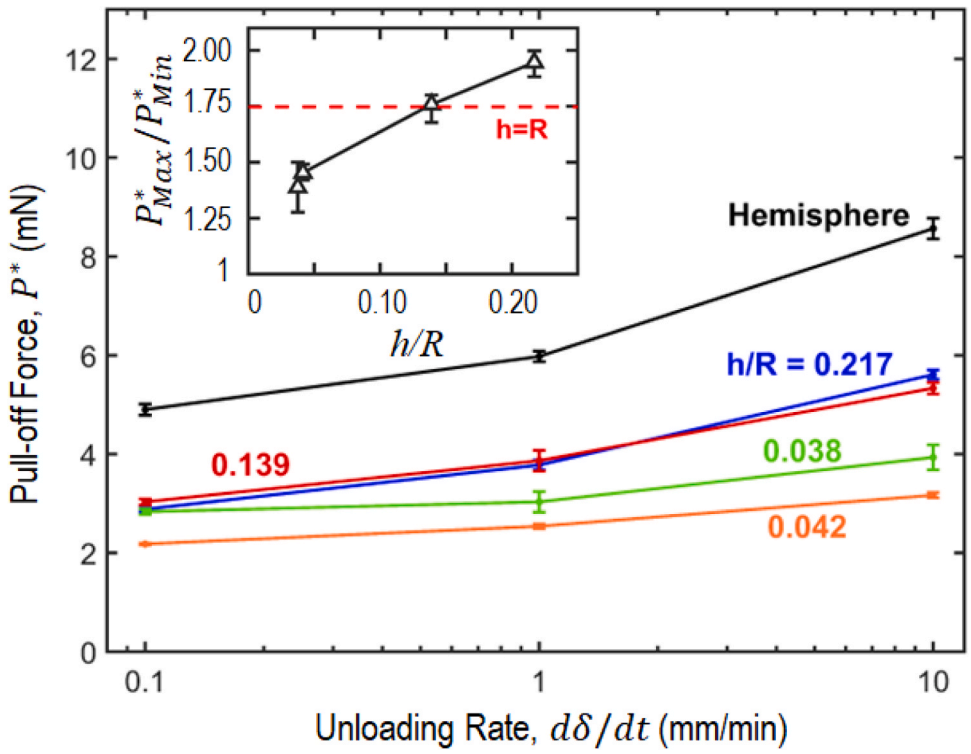

Fig. 7. Measured pull-off force in VPS-32 shells as a function of unloading speed for a range of shell thickness. Inset shows P^*_{Max}/P^*_{Min} where the subscripts *Max* indicating $d\delta/dt = 10$ mm/min and *Min* referring to $d\delta/dt = 0.1$ mm/min). The enhancement factor for hemisphere is measured as 1.75.

0.1 mm/min is chosen to be the lowest loading rate in this study. Defining $P^*_{Max} = P^*(d\delta/dt = 10\ \text{mm/min})$ and $P^*_{Min} = P^*(d\delta/dt = 0.1\ \text{mm/min})$, the ratio of $\varphi = P^*_{Max}/P^*_{Min}$ approaches unity if the shell material does not exercise viscoelasticity. All our samples show some degree of viscoelastic behavior. The inset graph shows φ as a function of (h/R). While a JKR solid yields $\varphi = 1.75$, the thinner the shell the smaller the measured φ. In the limit of $h = 0$, φ approaches 1.0.

It is worthwhile to compare Figs. 4c and 7. A very thin shell shows little dynamic behavior and dependency on loading rate. One reason is that energy is stored mainly by bending at the contact edge and a small contribution from the weak compression in the planar contact (c.f. Fig. 6). Contraction of the contact releases the energy. Conversely, the Hertz compression in a JKR solid contact stores up much elastic energy. An incremental increase in external tension thus releases a lot more energy in a JKR solid than a shell over a longer duration if the material possesses a finite loss modulus.

3.4. Implications for applications

The understanding of adhesion mechanics of thin elastomeric shells is crucial for design of adhesion-based soft grippers. Thin shells offer several distinct advantages over solid spheres and pillars with flat contact surfaces, especially in gripping delicate objects with irregular geometry. The compliance and flexibility of thin hemispherical shells allow more conformable contacts, ensuring better adhesion to complex and non-uniform surfaces.

Our previous studies have demonstrated the potential of using hollow pillar structures for dynamically tunable dry adhesion controlled by pneumatics [7,29]. An elastomeric post containing an annulus chamber has been shown to exhibit 5× dry adhesion change upon application of ~50 kPa pressure [29]. More recently, the use of shell buckling in soft hollow pillars induced by negative pressure to significantly reduce dry adhesion has also been explored [7]. This has resulted in switching ratios of dry adhesion strength up to 200× within fractions of a second, for soft hollow pillars made of VPS-8 with an adhesive strength of ~4 kPa when zero pressure is applied [7]. In comparison, the VPS-8 hemispherical shells in this study have adhesion forces of 2–5 mN (Fig. 5b), which can translate into a nominal adhesion strength of 0.01 kPa (normalized against the projected area of the hemisphere), more than two orders of magnitude lower than that of a hollow pillar ended with a flat membrane. This reduction in adhesion strength is particularly useful in manipulation of lightweight objects. It is also important to note here that in the ultrathin regime shell adhesion strength does not degrade significantly as shown in Fig. 5b, which allows for design flexibility.

In addition to characterizing the adhesion strength, this study enhances our fundamental understanding of mechanics of spherical shell adhesion, offering practical insights for designing adhesion-based grippers. For example, as demonstrated in Fig. 4d, thinner/softer shells exhibit a larger mechanical response (da/dP), indicating that the same change in adhesion force results in a more significant change in the contact radius for thinner/softer shells. This sensitivity in thinner/softer shells can potentially allow integration of soft vision-based haptic sensors [30], which can enable real-time tracking of adhesion force in delicate object handling operations.

4. Conclusion

We demonstrated in elastomeric shells how classical JKR model is insufficient to account for adhesion-delamination in thin shell where shell thickness plays a critical role in many ways: (i) a significantly larger contact area because the compliant shell conforms to the substrate geometry, (ii) bending-stretching deformation is present alongside the Hertz-JKR compression-tension, (iii) bending at the contact edge determines pull-off force, (iv) incremental increase in external tension shrinks the contact circle rapidly, and (v) viscoelastic behavior, if any at all, has small effect on the adhesion mechanics, albeit, a thin shell exercises a very different mechanical response, $P(a,\delta)$, that depends on shell thickness. These results provide insights in the design and operation of dry-adhesion-based soft robotic gripping systems.

CRediT authorship contribution statement

Chenxu Zhao: Writing – original draft, Visualization, Investigation, Formal analysis, Data curation. **Kai-tak Wan:** Writing – review & editing, Supervision, Project administration, Methodology, Formal analysis, Conceptualization. **Wanliang Shan:** Writing – review & editing, Supervision, Project administration, Investigation, Funding acquisition, Formal analysis, Conceptualization.

Declaration of Competing Interest

The authors declare the following financial interests/personal relationships which may be considered as potential competing interests: Wanliang Shan reports financial support was provided by National Science Foundation. N.A.

Data availability

Data will be made available on request.

Acknowledgements

The authors acknowledge the financial support by Syracuse University through startup fund for Wanliang Shan, and National Science Foundation award CMMI #2006430. Any opinions, findings, and conclusions or recommendations expressed in this material are those of the authors and do not necessarily reflect the views of NSF.

To prepare this manuscript, the author(s) used ChatGPT to touch up the writing. The authors reviewed and edited the script as needed and take full responsibility for the content.

Appendix A. Supporting information

Supplementary data associated with this article can be found in the online version at doi:10.1016/j.eml.2024.102140.

References

[1] M.-F. Wong, G. Duan, K.-T. Wan, Adhesion-delamination mechanics of a prestressed rectangular film adhered onto a rigid substrate, J. Appl. Phys. vol. 101 (2) (2007) 024903, https://doi.org/10.1063/1.2422775.
[2] T. Tang, A. Jagota, C.-Y. Hui, Adhesion between single-walled carbon nanotubes, J. Appl. Phys. vol. 97 (7) (2005) 074304, https://doi.org/10.1063/1.1871358.
[3] M.D. Kern, Y. Qi, R. Long, M.E. Rentschler, Characterizing adhesion between a micropatterned surface and a soft synthetic tissue, Langmuir vol. 33 (4) (2017) 854–864, https://doi.org/10.1021/acs.langmuir.6b03643.
[4] S. Sharifi, et al., Dynamically tunable friction via subsurface stiffness modulation, Front. Robot. AI vol. 8 (2021) 2021.
[5] A.M. Nasab, A. Sabzehzar, M. Tatari, C. Majidi, W. Shan, A soft gripper with rigidity tunable elastomer strips as ligaments, Soft Robot. vol. 4 (4) (2017) 411–420, https://doi.org/10.1089/soro.2016.0039.
[6] A. Mohammadi Nasab, P. Stampfli, S. Sharifi, A. Luo, K.T. Turner, W. Shan, Dynamically tunable dry adhesion through a subsurface thin layer with tunable stiffness, Adv. Mater. Interfaces vol. 9 (7) (2022) 2102080, https://doi.org/10.1002/admi.202102080.
[7] G. Wan, Y. Tang, K.T. Turner, T. Zhang, W. Shan, Tunable dry adhesion of soft hollow pillars through sidewall buckling under low pressure, Adv. Funct. Mater. vol. 33 (2) (2022) 2209905, https://doi.org/10.1002/adfm.202209905.
[8] G. Li, Y. Qiang, H. Li, X. Li, M. Dao, G.E. Karniadakis, An integrated in-silico and in-vitro microfluidic study of the adhesion dynamics of erythrophagocytosis in sickle cell disease, Biophys. J. vol. 0 (0) (2023), https://doi.org/10.1016/j.bpj.2023.05.022.
[9] J. Sun, R. Ran, S. Muftu, A.Z. Gu, K.-T. Wan, The mechanistic aspects of microbial transport in porous media, Colloids Surf. A Physicochem. Eng. Asp. vol. 603 (2020) 125169, https://doi.org/10.1016/j.colsurfa.2020.125169.
[10] J. Shi, S. Müftü, K.-T. Wan, Adhesion of a compliant cylindrical shell onto a rigid substrate, J. Appl. Mech. vol. 79 (4) (2012), https://doi.org/10.1115/1.4005555.
[11] J. Shi, S. Müftü, A. Gu, K.-T. Wan, Adhesion of a cylindrical shell in the presence of DLVO surface potential, J. Appl. Mech. vol. 80 (6) (2013), https://doi.org/10.1115/1.4023960.
[12] J. Shi, S. Müftü, K.-T. Wan, Adhesion of an elastic convex shell onto a rigid plate, J. Adhes. vol. 87 (6) (2011) 579–594, https://doi.org/10.1080/00218464.2011.583587.
[13] K.L. Johnson, K. Kendall, A.D. Roberts, D. Tabor, Surface energy and the contact of elastic solids, Proc. R. Soc. Lond. A Math. Phys. Sci. vol. 324 (1558) (1971) 301–313, https://doi.org/10.1098/rspa.1971.0141.
[14] B.V. Derjaguin, V.M. Muller, Y.P. Toporov, Effect of contact deformations on the adhesion of particles, J. Colloid Interface Sci. vol. 53 (2) (1975) 314–326, https://doi.org/10.1016/0021-9797(75)90018-1.
[15] D. Maugis, Adhesion of spheres: The JKR-DMT transition using a dugdale model, J. Colloid Interface Sci. vol. 150 (1) (1992) 243–269, https://doi.org/10.1016/0021-9797(92)90285-T.
[16] A.L. Flory, D.A. Brass, K.R. Shull, Deformation and adhesive contact of elastomeric membranes, J. Polym. Sci. Part B Polym. Phys. vol. 45 (24) (2007) 3361–3374, https://doi.org/10.1002/polb.21322.
[17] R. Long, K.R. Shull, C.-Y. Hui, Large deformation adhesive contact mechanics of circular membranes with a flat rigid substrate, J. Mech. Phys. Solids vol. 58 (9) (2010) 1225–1242, https://doi.org/10.1016/j.jmps.2010.06.007.
[18] X. Yang, A. Srivastava, R. Long, Adhesive contact of an inflated circular membrane with curved surfaces, Int. J. Solids Struct. vol. 279 (2023) 112371, https://doi.org/10.1016/j.ijsolstr.2023.112371.
[19] T. Zhu, G. Li, S. Müftü, K.-t Wan, Revisiting the constrained blister test to measure thin film adhesion, J. Appl. Mech. vol. 84 (071005) (2017), https://doi.org/10.1115/1.4036776.
[20] E. Reissner, Stresses and small displacements of shallow spherical shells. II, J. Math. Phys. vol. 25 (1-4) (1946) 279–300, https://doi.org/10.1002/sapm1946251279.
[21] W. Wang, J.V. Gray, S.E. Julien, K.T. Wan, Mechanical characterization of a convex shell (Contact Lens) with meridional thickness variation, Exp. Mech. vol. 58 (6) (2018) 997–1002, https://doi.org/10.1007/s11340-018-0400-9.
[22] C. Zhao, X. Chen, W. Shan, K.-T. Wan, Adherence of a hyperelastic shell on a rigid planar substrate, Int. J. Solids Struct. vol. 236-237 (2022) 111351, https://doi.org/10.1016/j.ijsolstr.2021.111351.
[23] J. Marthelot, F. López Jiménez, A. Lee, J.W. Hutchinson, P.M. Reis, Buckling of a pressurized hemispherical shell subjected to a probing force, J. Appl. Mech. vol. 84 (12) (2017), https://doi.org/10.1115/1.4038063.
[24] A. Lee, P.T. Brun, J. Marthelot, G. Balestra, F. Gallaire, P.M. Reis, Fabrication of slender elastic shells by the coating of curved surfaces, Nat. Commun. vol. 7 (1) (2016) 11155, https://doi.org/10.1038/ncomms11155.
[25] M. Liu, J. Sun, Y. Sun, C. Bock, Q. Chen, Thickness-dependent mechanical properties of polydimethylsiloxane membranes, J. Micromech. Microeng. vol. 19 (3) (2009) 035028, https://doi.org/10.1088/0960-1317/19/3/035028.
[26] J.W. Hutchinson, Z. Suo, Mixed mode cracking in layered materials, Adv. Appl. Mech. vol. 29 (1991) 63–191, https://doi.org/10.1016/S0065-2156(08)70164-9.
[27] M.D. Swift, C.B. Haverkamp, C.J. Stabile, D. Hwang, R.H. Plaut, K.T. Turner, D. A. Dillard, M.D. Bartlett, Active membranes on rigidity tunable foundations for programmable, rapidly switchable adhesion, Adv. Mater. Technol. vol. 5 (11) (2020) 2000676, https://doi.org/10.1002/admt.202000676.
[28] X. Feng, M.A. Meitl, A.M. Bowen, Y. Huang, R.G. Nuzzo, J.A. Rogers, Competing fracture in kinetically controlled transfer printing, Langmuir vol. 23 (25) (2007) 12555–12560, https://doi.org/10.1021/la701555n.
[29] A. Mohammadi Nasab, A. Luo, S. Sharifi, K.T. Turner, W. Shan, Switchable adhesion via subsurface pressure modulation, ACS Appl. Mater. Interfaces vol. 12 (24) (2020) 27717–27725, https://doi.org/10.1021/acsami.0c05367.
[30] H. Sun, K.J. Kuchenbecker, G. Martius, A soft thumb-sized vision-based sensor with accurate all-round force perception, Nat. Mach. Intell. vol. 4 (2) (2022) 135–145, https://doi.org/10.1038/s42256-021-00439-3.